

Production and Precipitation Hardening of Beta-Type Ti-35Nb-10Cu Alloy Foam for Implant Applications

Ilven Mutlu, Sinem Yenyol, and Enver Oktay

(Submitted January 30, 2015; in revised form January 3, 2016; published online March 4, 2016)

In this study, beta-type Ti-35Nb-10Cu alloy foams were produced by powder metallurgy method for dental implant applications. 35% Nb was added to stabilize the beta-Ti phase with low Young's modulus. Cu addition enhanced sinterability and gave precipitation hardening capacity to the alloy. Sintered specimens were precipitation hardened in order to enhance the mechanical properties. Electrochemical corrosion behavior of the specimens was examined by electrochemical impedance spectroscopy in artificial saliva. Electrochemical impedance spectroscopy results indicated that the oxide film on the surface of foam is a bi-layer structure consisting of outer porous layer and inner barrier layer. Impedance values of barrier layer were higher than porous layer. Corrosion resistance of specimens decreased at high fluoride concentrations and at low pH of artificial saliva. Corrosion resistance of alloys was slightly decreased with aging. Mechanical properties, microstructure, and surface roughness of the specimens were also examined.

Keywords artificial saliva, beta-ti, dental implant, EIS method, Ti-35Nb-10Cu

1. Introduction

Porous materials exhibit a structure similar to cancellous bone. Advantage of the porous metals is their ability to provide anchorage for the surrounding tissue via ingrowth of tissue into their pores. Implants suffer from mismatch of their Young's modulus with bone (Ref 1–5). Ti alloys are used in biomedical applications because of their high strength to density ratio, biocompatibility, and corrosion resistance. However, there are disadvantages such as high Young's modulus and low wear resistance (Ref 3–6). Ti has hexagonal close-packed (α -phase) structure at room temperature and transforms to body-centered cubic beta structure (β -phase) at 883 °C, which can be increased by α -phase stabilizers (Al, O, N) or lowered by beta (β)-phase stabilizers (Mo, Nb, Ta, V). Beta-Ti phase has low Young's modulus (close to bone), high wear resistance, and biocompatibility (Ref 7–13). Nb is non-toxic, biocompatible, and it is a beta-Ti stabilizer. Moreover, some Ti-Nb alloys exhibit shape memory effect (Ref 14–16).

Cu addition enhances sinterability of the Ti particles, and compacts were sintered at lower temperatures than other Ti alloys. Addition of Cu contributes to easier machining. Cu addition also enhances heat treatment capacity by aging (Ref 17–22). As a bioinert material, titanium alloys do not have antibacterial capability after implantation in the jaws, and dental plaques can be identified around Ti dentures. Bacterial colonization leads to implant loosening through the stages of peri-implantitis (Ref 23, 24). It is important to develop

functional transmucosal implant surfaces that inhibit colonization of the oral bacteria (Ref 25). Antibacterial activity is affected by surface properties of the implants. Several metal ions (Ag^+ , Cu^{2+} , and Zn^{2+}) were used as antibacterial agents. Cu represents a promising element in terms of its lower toxicity. Furthermore, Cu is a metabolizable agent whereas Ag^+ tends to stay in the human body. Ti-Cu alloy is considered as a candidate dental implant material with respect to its antibacterial activity and biocompatibility. Antibacterial activity is affected by surface properties of the implants. Poor adhesive strength leads to failing of antibacterial coating, which would result in loss of antibacterial properties. It is important to develop a material, which has antibacterial activity in its bulk structure rather than on its surface (Ref 22–25).

In this study, beta-Ti type heat treatable Ti-35Nb-10Cu alloy foams were produced for dental implant applications. Beta-Ti alloys have low Young's modulus similar to the cancellous bone. Although cast Ti-Cu alloy and powder metallurgy-based Ti-Nb alloys have been studied, there is no study on the powder metallurgy-based heat-treatable beta-type Ti-35Nb-10Cu alloy foam in the literature. Experimental studies on corrosion behavior of beta-Ti alloy system are also scarce. The aim of the present work was the production of Ti-35Nb-10Cu alloy foam and characterization of the corrosion properties by EIS method. In short, there is no study on powder metallurgy-based highly porous Ti-35Nb-10Cu alloy foam. In addition, studies on corrosion behavior of beta-Ti alloys are scarce.

2. Experimental

2.1 Specimen Production

Foams were produced by powder metallurgy-based space holder method using Ti, Nb, and Cu powders (Alfa Aesar, USA). Chemical composition of the Ti powder was 99.61 wt.% Ti, 0.23 wt.% O, 0.018 wt.% N, 0.03 wt.% Fe, 0.01 wt.% Mn, 0.01 wt.% Mg, 0.009 wt.% C, <0.01 wt.% Al, 0.01 wt.% Cl, <0.01 wt.% Na and 237 ppm H. Nb powder consisted of 99.8 wt.% Nb, while Cu powder consisted of 99.75 wt.% Cu

Ilven Mutlu and **Enver Oktay**, Metallurgical and Materials Engineering Department, Istanbul University, Istanbul, Turkey; and **Sinem Yenyol**, Department of Oral Implantology, Faculty of Dentistry, Istanbul University, Istanbul, Turkey. Contact e-mail: imutlu@istanbul.edu.tr.

and 0.10 wt.% O. Mean particle sizes of the Ti, Cu, and Nb powders were 44, 34, and 34 μm , respectively. In the alloy preparation stage, 35 wt.% Nb and 10 wt.% Cu powder were added to the Ti powder. As a space holder, carbamide (Merck, Germany), in the fraction of 710 to 1000 μm , was used. The urea percentage in the mixture was about 55 and 80 vol.%. Binder for green strength was polyvinylalcohol (PVA). Metal powders were mixed with 1.5 wt.% PVA. Mixtures were compacted at 200 MPa into cylindrical specimens with diameter of 12 mm and heights of 15 to 20 mm. Specimens were immersed in water and then carbamide was leached out. PVA was thermally removed at 400 °C. Sintering consisted of heating at a rate of 5 °C/min to 410 °C (debinding) with dwell time of 40 min, followed by heating at rate of 11 °C/min to sintering temperatures. Specimens were sintered at temperatures between 1000 and 1250 °C for 45 min in pure argon atmosphere in a tube furnace. Optimum sintering temperature was determined as 1200 °C. The specimens were sintered at 1200 °C for 45 min. In the precipitation hardening (aging) step, sintered specimens were initially solution treated at 1000 °C in a vacuum furnace and then quenched using N_2 as a cooling gas in the same furnace. Quenched specimens were subsequently aged at 480 °C.

2.2 Artificial Saliva Preparation

Artificial saliva solution was prepared from chemicals supplied by Merck, Germany (Ref 4, 26–28). Amounts of the reagents were 0.40 g/l NaCl, 0.79 g/l $\text{CaCl}_2 \cdot \text{H}_2\text{O}$, 0.40 g/l KCl, 0.005 g/l $\text{Na}_2\text{S} \cdot 9\text{H}_2\text{O}$, 0.78 g/l $\text{NaH}_2\text{PO}_4 \cdot \text{H}_2\text{O}$, 0.35 g/l Urea- $\text{CO}(\text{NH}_2)_2$. In the oral environment, in which pH varies between 2 and 11, F^- concentration has effects on implants. There is increased use of gels containing fluoride to prevent plaque and caries (Ref 29, 30). In order to determine effect of fluoride on our specimens, artificial saliva with 0.25, 0.50, 0.75, and 1.00 wt.% F^- was prepared via NaF addition. pH was adjusted to 2.50, 5.00, and 7.40 by adding lactic acid.

Metal ion release from the alloys was investigated by static immersion tests in the artificial saliva solution. Inductively coupled plasma-mass spectrometer, ICP-MS, (Thermo Scientific Elemental X Series 2) was used to determine metal ion release. Specimens with 70% porosity were machined, polished, and washed, respectively. Total porosity and surface area values of the specimens were equal in the static immersion tests. Specimens were then exposed to artificial saliva solution in closed polyethylene bottles. Foams with equal porosity levels were immersed in solution at room temperature for several soaking times up to 14 days. Solution volume to specimen surface area ratio was constant in the immersion tests. A solution without a specimen was used for blank test.

2.3 Electrochemical Corrosion Study

Electrochemical corrosion studies were carried out in the artificial saliva using a potentiostat (Interface 1000 Potentiostat/Galvanostat/ZRA, Gamry Instruments Inc., USA) controlled by a personal computer. Volume of glass corrosion test cell was 1000 mL. A conventional three-electrode system with high-density graphite rod as a counter electrode, a saturated calomel electrode (SCE) as reference electrode, and specimen as a working electrode was used. Data acquisition was carried out through a computer software (Framework, Version 6.04, Gamry Instruments, USA), while data analysis was carried out

by Echem Analyst Software, Version 6.04, Gamry Instruments, USA. Specimens were prepared by being cut and then mounted into epoxy resin. The specimens were connected to a copper wire. All experiments were carried out at room temperature. Open circuit potential (OCP) value of the specimens was measured before carrying out the electrochemical corrosion experiments. OCP level was measured for the durations of 2 to 3 h, until the OCP value was stabilized. OCP value was considered stable when the OCP curve has an asymptotically stable region. The OCP value was also considered stable when the OCP was not changed at a rate of 3 mV/min or higher.

Electrochemical impedance spectroscopy (EIS) measurements were started after each specimen reaches a steady-state condition. Electrochemical impedance spectroscopy measurements were carried out in potentiostatic mode, at OCP with a constant voltage perturbation a.c. sine wave. The potential amplitude of signal was 5 mV. EIS studies were conducted at a frequency range from 100 kHz to 0.001 Hz, with 5 points per frequency decade. Impedance spectra were fitted by an electrical equivalent circuit model using Gamry, EIS100 software, by a complex non-linear-least-square method. Quality of the fit was described by the average error of regression. Nyquist and Bode spectra were recorded.

2.4 Characterization of Microstructure and Mechanical Properties

Densities were determined from measurements of weights and dimensions of the specimens. SEM images of the specimens were used to determine the mean pore size and pore shape. X-ray diffraction (XRD) analysis (Rigaku D/Max-2200/PC) was also used in order to characterize the alloys. Mechanical properties of the specimens were studied by the compression tests performed on a Shimadzu AG-X materials testing machine. Compression tests were carried out at a crosshead speed of 0.5 mm/min. The stress was calculated using the apparent cross-sectional area of the respective specimen; Young's modulus was determined from the slope of linear portion of the elastic region of the corresponding stress-strain graph by the software. Surface roughness parameters (average roughness R_a , maximum height of the profile, R_t and average maximum height of the profile, R_z) of the specimens were also determined (Mitutoyo, SurfTest SJ-301).

3. Results and Discussion

3.1 Foam Structure

Ti-35Nb-10Cu alloy foams were produced by powder metallurgy-based space holder method. Pore size and pore morphology of the foams replicated initial size and morphology of the carbamide (space holder) particles and the mean pore sizes of the foams were about 450 to 500 μm , which are suggested as the suitable range of values for biomedical implant (hard tissue) applications (Ref 3–5). Figure 1 shows the SEM image of the cracked surface of the foam with about 70% porosity. As seen from the Fig. 1, some micropores are found inside the macropores, which suggest that the macropores are connected by small microchannels for the escape of gas during sintering. In general, a certain amount of micropores are desired for vascularization in the biomedical implants.

3.2 Electrochemical Impedance Spectroscopy Study

Equivalent electric circuit with two time constants is used to analyze the electrochemical impedance spectroscopy (EIS) data and to interpret behavior of the alloy and its surface oxide film. Figure 2 shows the equivalent electric circuit, $R_{sol}(C_{pore}(R_{pore}(C_{barr}R_{barr})))$, to fit the EIS data. Model assumes that the passive oxide layer consists of a barrier-like inner layer and a porous outer layer. The R_{sol} represents electrolyte (solution) resistance, and constant phase element (C) representing shift from ideal capacitor is used instead of capacitance. R_{pore} and R_{barr} are resistances of porous and barrier layers that are associated with charge transfer resistance through porous layer and participation of adsorbed intermediates. C_{pore} and C_{barr} correspond to capacitances of porous and barrier layers which are related to double layer formation. Fitting quality of the EIS data is judged by Chi-squared (χ^2) values of about 10^{-6} , indicating a good fitting to proposed equivalent electrical circuit. The n values close to one indicate near capacitive behavior of the passive oxide film. The n value is associated with non-uniform distribution of the current as a result of surface roughness and surface defects.

Experimental and simulated impedance spectra of the foams are presented as Nyquist and Bode plots. Nyquist plot is characterized by a semicircle, indicating capacitive response of

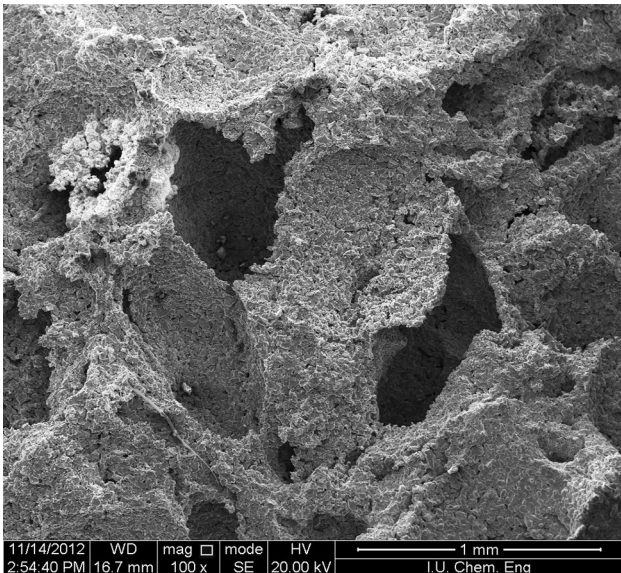


Fig. 1 SEM image of cracked surface of the foam

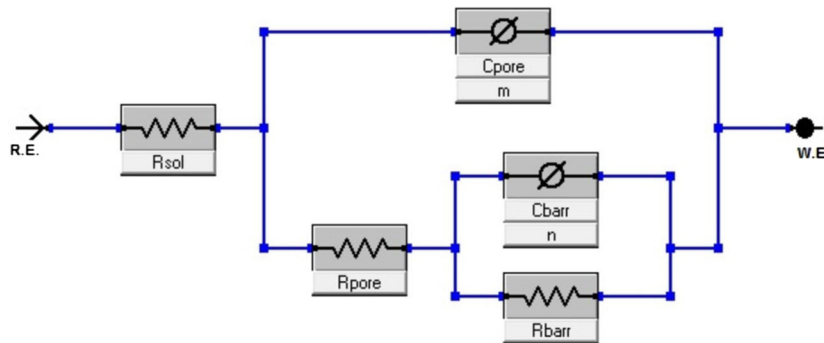


Fig. 2 Equivalent electric circuit to fit the EIS data

the passive film. Bode magnitude plots are characterized by two regions. In high frequency, there is flat portion due to electrolyte resistance. In low frequency, impedance shows a linear slope due to capacitive behavior. Bode phase plots show different behaviors. There are three regions in the Bode phase plots. In high frequency, phase angle drops toward 0° due to electrolyte resistance. In middle frequency, phase angle remains near -50° indicating passive film and its capacitive response. In low frequency, phase angle decreases because of passive film resistance. Phase angle approaching -90° indicates passive film and capacitive response. Constant phase angle maximum over a wide frequency range suggests formation of stable passive film and difficulty in charge transfer. Two phase angle peaks are indicative of two relaxation time constants and formation of a two-layer (duplex) passive oxide film.

Resistances of inner barrier layer (R_{barr}) are higher than outer porous layer (R_{pore}) demonstrating that inner layer dominates corrosion protection. Higher impedance, lower capacitances, and larger phase angle are attributed to nobler electrochemical corrosion behavior.

3.2.1 Effect of Precipitation Hardening (Aging). Figure 3 shows the effect of aging (precipitation hardening) treatment on the Nyquist plots of the specimens, while Fig. 4 illustrates the effect of aging (precipitation hardening) on the (a) Bode magnitude (Z_{mod}), and (b) Bode phase angle plots of the specimens. As seen from Fig. 3, lower capacitive open semi-arc diameters can be observed for precipitation hardened

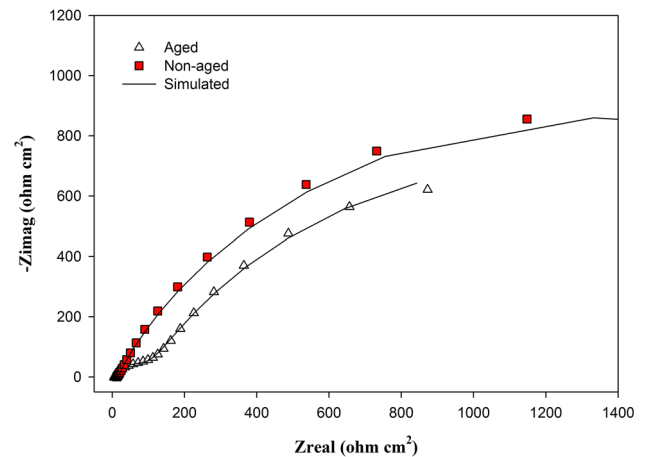


Fig. 3 Effect of aging on the Nyquist plots of the specimens (pH 7.40, 0.50% F, 52% porosity, 10% Cu)

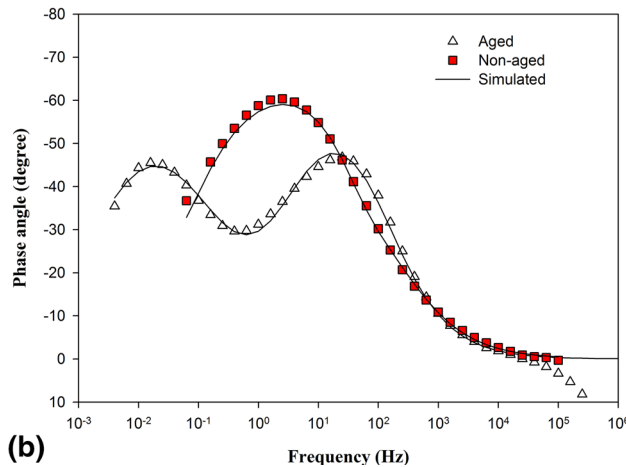
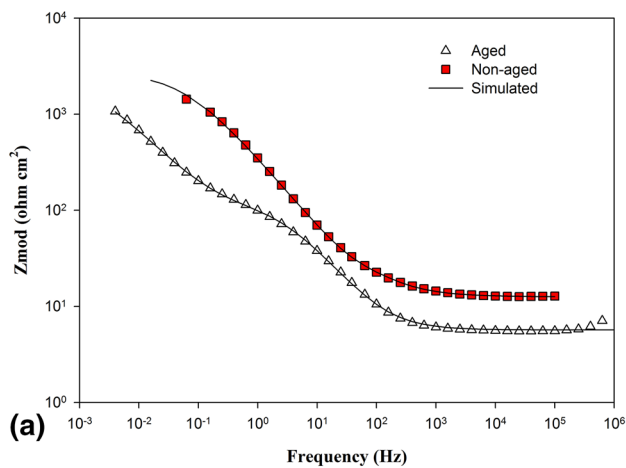


Fig. 4 Effect of aging on the (a) Bode magnitude and (b) Bode phase angle plots of the specimens (pH 7.40, 0.50% F, 52% porosity, 10% Cu)

(aged) specimens in Nyquist plots. Low capacitances can be associated with increase in passive layer thickness and decrease in dielectric constant of the oxide film. As shown in Fig. 4, in higher frequency, Bode magnitude plots were exhibited near constant Z_{mod} , associated with phase angle near zero degree, indicating that the impedance was dominated by electrolyte resistance. On the other hand, in low and middle frequency, Bode magnitude displayed linear slope, due to capacitive behavior (Ref 31–33). In the Bode phase plots, in high frequency, phase angle drops toward 0° due to electrolyte resistance. In middle frequency, phase angle remains near -60° indicating passive film and its capacitive response. In low frequency, phase angle decreases because of passive film resistance.

3.2.2 Effect of Fluoride Content and pH of Artificial Saliva. Electrochemical impedance spectroscopy (EIS) measurements were carried out at different F at pH values of artificial saliva. Figure 5 shows the effect of pH of the artificial saliva on the Nyquist plots of the specimens, while Fig. 6 illustrates the effect of pH of artificial saliva on the (a) Bode magnitude, and (b) Bode phase angle plots of the specimens. As seen in Fig. 5, capacitive semicircles were observed in the Nyquist plots of the specimens. The sizes of the semicircles were decreased as the pH value of the artificial saliva decreased. The Nyquist plot was composed of two semicircles.

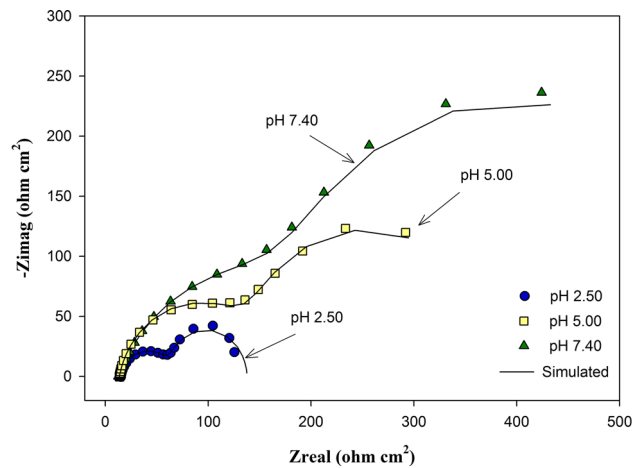


Fig. 5 Effect of pH of the artificial saliva on the Nyquist plots of the specimens (1.00% F, 78% porosity, 10% Cu, nonaged)

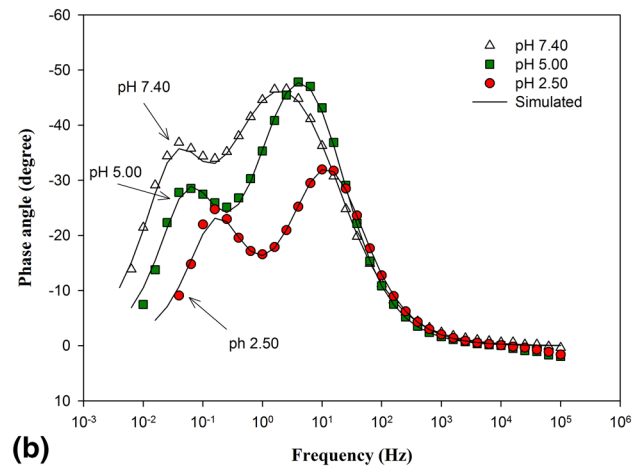
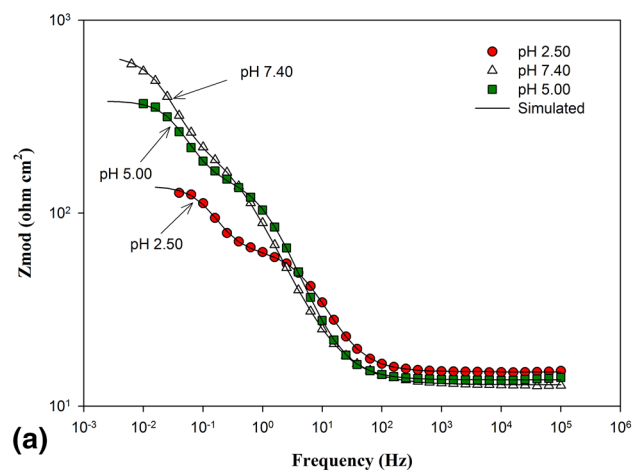


Fig. 6 Effect of pH of artificial saliva on the (a) Bode magnitude, and (b) Bode phase angle plots of the specimens (1.00% F, 78% porosity, 10% Cu, nonaged)

As shown in Fig. 6(a), in higher frequency, Bode magnitude plots were exhibited constant Z_{mod} , associated with phase angle near zero degree, indicating that impedance was dominated by electrolyte resistance. In low frequency, Bode magnitude

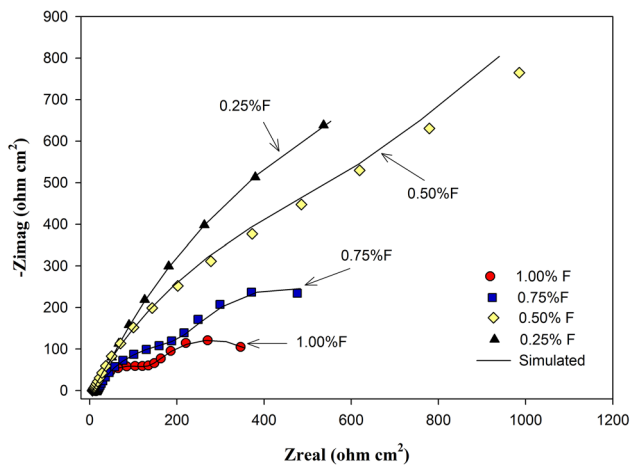


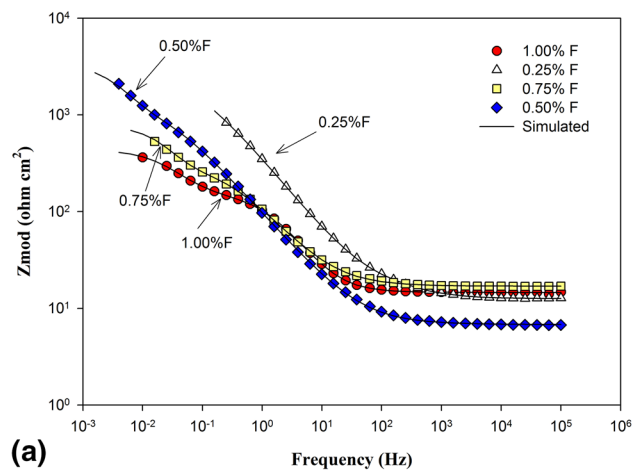
Fig. 7 Effect of F content of the artificial saliva on the Nyquist plots of the specimens (pH 7.40, 52% porosity, 10% Cu, nonaged)

displayed linear slope, due to capacitive behavior. In the Bode phase plots, in high frequency, phase angle drops toward 0° due to electrolyte resistance. In middle frequency, phase angle remains about -50° indicating capacitive response. In low frequency, phase angle decreases because of film resistance. As seen from the Fig. 6(a), magnitude values were decreased with decreasing pH level of artificial saliva. In the Bode phase plots in Fig. 6(b), phase angle drops toward 0° in high frequency due to electrolyte resistance. In middle frequency, phase angle remains near -50° indicating capacitive response. Phase angle was decreased with decreasing pH level of artificial saliva.

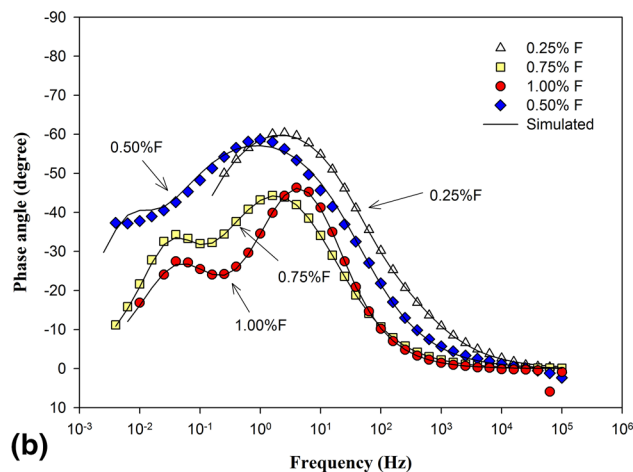
Figure 7 shows the effect of F^- content of the artificial saliva on the Nyquist plots of the specimens. Figure 8 illustrates the effect of F^- content of artificial saliva on the (a) Bode magnitude, and (b) Bode phase angle plots of the specimens. As seen in Fig. 7, capacitive semicircles were observed in the Nyquist plots of the specimens. The sizes of the semicircles were decreased as the F content of the artificial saliva increased. As seen from Fig. 8(a), magnitude values were decreased with increasing F^- content of the artificial saliva. Phase angle values were also decreased with increasing F^- content of the artificial saliva.

Dissolution of the Ti is due to formation of Ti-F complex. Incorporation of the F in the surface oxide film results in formation of a porous layer. Depending on the concentration of the F and pH, titanium fluoride, titanium oxyfluoride, or sodium titanium fluoride may form. HF is responsible for destroying the passive oxide film. Once the passive layer is destroyed, regeneration of passive layer is a function of the dissolved oxygen. Electrochemical behavior of the titanium in F^- added acidic solutions was determined by the presence of HF. In low pH conditions, HF leads to destruction of the passive oxide. There are two kinds of fluoride in solutions, HF and F. Both can affect the electrochemical corrosion resistance of the titanium. Porosity of film is increased by F^- and low pH, due to the dissolution (Ref 32–36).

Electrical parameters fitted by equivalent circuit model are listed in Table 1. Specimens show lower R values in artificial saliva with low pH, which can be confirmed by smaller and deformed semicircles. In addition, lower frequency semicircles in the Nyquist plots represent exposed internal surface area. Resistances of inner barrier layer (R_{barr}) are higher than outer porous layer (R_{pore}) demonstrating that inner layer dominates corrosion protection behavior. Capacitances decrease and



(a)



(b)

Fig. 8 Effect of F content of artificial saliva on the (a) Bode magnitude, and (b) Bode phase angle plots of the specimens (pH: 7.40, 52% porosity, 10% Cu, nonaged)

resistances increased with increasing pH. Passive oxide film becomes more resistive with increasing pH.

3.3 Metal Ion Release Behavior

Fluoride-containing toothpastes and mouth rinses, which are recommended for preventing plaque and caries, tend to corrode Ti alloy implants or restorations, if they are used in acidic environment (Ref 37). It is a vital requirement to improve the corrosion resistance and develop the mechanical strength of dental implant materials. Cumulative Cu ion concentration in the artificial saliva solution was increased with increasing Cu content of the implant alloy and with immersion time. Ti alloys with high Cu content exhibited higher Cu ion release in artificial saliva. According to the static immersion study, decreasing pH level of the artificial saliva solution had increased the metal (Cu) ion release. Decreasing pH of the artificial saliva solution from 7.40 to 2.50 had increased the Cu ion release from about 40–50 to 80–100 ppb. In order to determine the effect of F concentration of the artificial saliva, artificial saliva solutions with different F^- concentrations were prepared. Increasing F^- content of artificial saliva solution from 0 to 1 wt.% had increased the metal ion (Cu) release. Meanwhile, metal ion release values of the specimens were not higher than reference levels of the ions in human body

Table 1 Electrochemical impedance spectroscopy parameters of the alloy obtained by fitting by equivalent electrical circuit model

pH	$R_{sol}, \Omega \text{ cm}^2$	$R_{pores}, \Omega \text{ cm}^2$	$C_{pores}, \text{S s}^a/\text{cm}^2$	n	$R_{barr}, \Omega \text{ cm}^2$	$C_{barr}, \text{S s}^a/\text{cm}^2$	m	χ^2
7.40	$17 \pm 0,10$	169 ± 12	0.005 ± 0.0001	0.96 ± 0.06	501 ± 66	0.015 ± 0.001	0.60 ± 0.07	94×10^{-6}
5.00	4 ± 0.08	157 ± 12	0.003 ± 0.0001	0.94 ± 0.05	270 ± 57	0.015 ± 0.001	0.74 ± 0.08	94×10^{-6}
2.50	14 ± 0.10	130 ± 11	0.002 ± 0.0001	0.99 ± 0.06	165 ± 49	0.018 ± 0.001	0.72 ± 0.08	16×10^{-6}

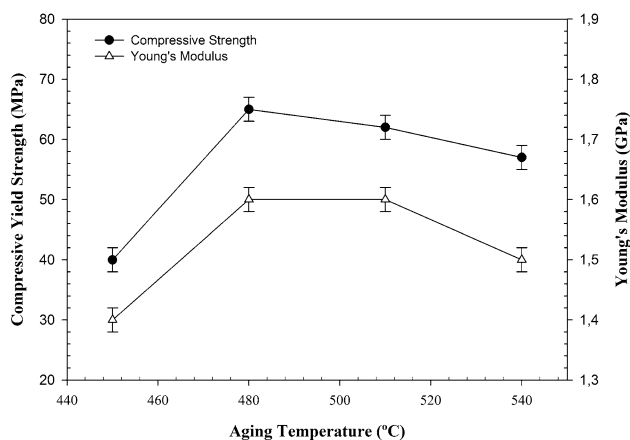


Fig. 9 Effect of aging temperature on the mechanical of the specimens

fluids (Ref 21, 36). Increased release of Cu with the increased F^- concentrations and with the increasing acidic environment indicates a positive influence on antibacterial levels of Cu for the transmucosal implants vulnerable to bacterial contamination. As a bioinert material, titanium alloys do not have antibacterial capability after implantation, and dental plaques can be identified around implanted Ti dentures. Bacterial infections are reason for complications of Ti-based implants. Implants with antibacterial activity must be used in order to reduce the infection. Ti alloy with Cu addition has biocompatibility and corrosion resistance for dental implants. Ti-Cu alloy is considered as a candidate dental implant material and shows antibacterial activity (Ref 22).

3.4 Microstructure and Mechanical Properties

Young's modulus and compressive yield strength of the specimens were increased with increasing aging (precipitation hardening) temperature and have reached its peak at about 480 to 490 °C and then decreased. This was attributed to the formation of coherent Cu-rich precipitates (Ti_2Cu) in optimum sizes. Hardening was attributed to pinning of dislocations by precipitated clusters. Decrease in the mechanical properties with overaging was attributed to formation of coarse and incoherent precipitates. Initially, increasing aging temperature up to 480 °C increased the compressive yield strength of the specimens from 40 to 65 MPa. Increasing aging temperature also increased the Young's modulus from 1.40 to 1.60 GPa. But increasing temperature above 480 °C decreased the Young's modulus and compressive yield strength from peak values to 1.50 GPa and 57 MPa, respectively. Maximum Young's modulus and compressive yield strength values of the aged 60% porous specimens were 1.60 GPa and 65 MPa, respectively. Young's modulus and compressive yield strength values

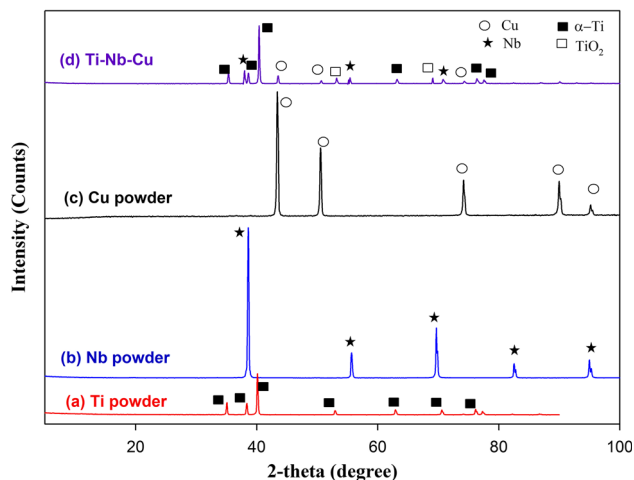


Fig. 10 XRD patterns of the (a) Ti powder, (b) Nb powder, (c) Cu powder, and (d) sintered Ti-35Nb-10Cu alloy

were decreased with increasing porosity. Young's modulus and compressive yield strength of aged 79% porous specimens were 0.56 GPa and 25 MPa, respectively. Figure 9 shows the effect of precipitation hardening (aging) temperature on the mechanical properties (compressive yield strength and Young's modulus) of the specimens.

Increase in the Young's modulus during initial stages of aging was attributed to the increase in Young's modulus of matrix due to depletion of Cu and to formation of coherent precipitates in optimum sizes. Increase was also attributed to the increased fraction of precipitates, which reduced the distortion. In overaged condition, loss of coherency leads to decrease in the Young's modulus. The Young's modulus depends on crystal structure, alloying, and phases. Young's modulus of an alloy is determined by elastic modulus and volume fractions of its phases. Aging promotes precipitation of the clusters and variations of the microstructure, which varies the Young's modulus (Ref 17, 18).

Figure 10 shows the XRD patterns of the (a) Ti powder, (b) Nb powder, (c) Cu powder, and (d) sintered Ti-35Nb-10Cu alloy. As-received titanium powder consists of alpha titanium phase. Sintered alloy mainly consists of alpha titanium. Some oxide (TiO_2) was also formed on the surfaces of the sintered specimens.

In general, biomedical implant (orthopaedic or dental) materials for load bearing (bone replacement) applications are fabricated to have sufficiently rough surface to increase contact area with the surrounding tissues. Moreover, cell viability is dependent on the surface roughness of the implant material on which the cells are attached. In the present study, the average roughness (R_a) of the specimens was about 10 μm , which is a suitable value for implant applications (Ref

36). In addition, maximum height (R_1) and average maximum height (R_2) values are measured and found to be 20 and 24 μm , respectively.

4. Conclusions

Beta-type Ti-35Nb-10Cu alloy for dental implant applications was produced by powder metallurgy technique. Cu addition enhanced the sinterability and Cu-added compacts were sintered at lower temperatures than the traditional Ti alloys, due to the low melting point of the alloy. The electrochemical impedance spectroscopy (EIS) results indicated that the passive oxide film formed on the surface of the foam is a bi-layer structure consisting of an outer porous layer and an inner barrier layer. Electrochemical impedance values of the barrier layer were higher than porous layer demonstrating that the inner barrier layer ensured the foam with a good electrochemical corrosion resistance. Increased fluoride concentration of the artificial saliva reduces its corrosion protection behavior. Fluoride ions attack the alloys, and severity of this attack depends on its concentration and pH level of the artificial saliva. Electrochemical corrosion resistance of the specimens decreases at high F concentrations and at low pH levels. Electrochemical corrosion resistance of the alloys was slightly decreased with precipitation hardening (aging). Diameters of the capacitive open semi-arcs in Nyquist plots decreased with aging.

Acknowledgments

This work was supported partially by Scientific Research Projects Coordination Unit of Istanbul University, Project Number 42922.

References

1. M.F. Ashby, A.G. Evans, N.A. Fleck, L.J. Gibson, J.W. Hutchinson, and H.N.G. Wadley, *Metal Foams: A Design Guide*, Elsevier Science, Boston, 2000
2. L.J. Gibson and M.F. Ashby, *Cellular Solids-Structures and Properties*, 2nd ed., Cambridge University Press, Cambridge, 1997
3. N. Wenjuan, B. Chenguang, Q. GuiBao, and W. Qiang, Processing and Properties of Porous Titanium Using Space Holder Technique, *Mater. Sci. Eng. A*, 2009, **506**, p 148–151
4. I. Mutlu and E. Oktay, Characterization of 17-4 PH Stainless Steel Foam for Biomedical Applications in Simulated Body Fluid and Artificial Saliva, *Mater. Sci. Eng. C*, 2013, **33**, p 1125–1131
5. L.J. Gibson, Biomechanics of Cellular Solids, *J. Biomech.*, 2005, **38**, p 377–399
6. J.G. Lin, Y.C. Li, C.S. Wong, P.D. Hodgson, and C.E. Wen, Degradation of the Strength of Porous Titanium After Alkali and Heat Treatment, *J. Alloy Compd.*, 2009, **485**, p 316–319
7. J. Huang, H. Xing, and J. Sun, Structural Stability and Generalized Stacking Fault Energies in β Ti–Nb Alloys: Relation to Dislocation Properties, *Scripta Mater.*, 2012, **66**, p 682–685
8. Q. Wei, L. Wang, Y. Fu, J. Qin, W. Lu, and D. Zhang, Influence of Oxygen Content on Microstructure and Mechanical Properties of Ti–Nb–Ta–Zr Alloy, *Mater. Des.*, 2011, **32**, p 2934–2939
9. S.A. Souza, R.B. Manicardi, P.L. Ferrandini, C.R.M. Afonso, A.J. Ramirez, and R. Caram, Effect of the Addition of Ta on Microstructure and Properties of Ti–Nb Alloys, *J. Alloy Compd.*, 2010, **504**, p 330–340
10. D.C. Zhang, Y.F. Mao, Y.L. Li, J.J. Li, M. Yuan, and J.G. Lin, Effect of Ternary Alloying Elements on Microstructure and Superelasticity of Ti–Nb Alloys, *Mater. Sci. Eng. A*, 2013, **559**, p 706–710
11. E.S.N. Lopes, A. Cremasco, C.R.M. Afonso, and R. Caram, Effects of Double Aging Heat Treatment on the Microstructure, Vickers Hardness and Elastic Modulus of Ti–Nb Alloys, *Mater. Charact.*, 2011, **62**, p 673–680
12. Z.C. Zhou, J.Y. Xiong, S.Y. Gu, D.K. Yang, Y.J. Yan, and J. Du, Anelastic Relaxation Caused by Interstitial Atoms in β -type Sintered Ti–Nb Alloys, *J. Alloy Compd.*, 2011, **509**, p 7356–7360
13. W. Xiao-jun, Effects of Alkali and Heat Treatment on Strength of Porous Ti35Nb, *Trans. Nonferrous Met. Soc. China*, 2011, **21**, p 1335–1339
14. V. Raman, S. Nagarajan, and N. Rajendran, Electrochemical Impedance Spectro-Scopic Characterisation of Passive Film Formed Over Ti-29Nb-13Ta-4.6Zr Alloy, *Electrochem. Commun.*, 2006, **8**, p 1309–1314
15. B.L. Wang, Y.F. Zheng, and L.C. Zhao, Electrochemical Corrosion Behavior of Biomedical Ti-22Nb and Ti-22Nb-6Zr Alloys in Saline Medium, *Mater. Corros.*, 2009, **60**(10), p 788–794
16. A. Cremasco, W.R. Osorio, C.M.A. Freire, A. Garcia, and R. Caram, Electrochemical Corrosion Behavior of a Ti-35Nb Alloy for Medical Prostheses, *Electrochim. Acta*, 2008, **53**, p 4867–4874
17. X. Yao, Q.Y. Sun, L. Xiao, and J. Sun, Effect of Ti₂Cu Precipitates on Mechanical Behavior of Ti–2.5Cu Alloy Subjected to Different Heat Treatments, *J. Alloy Compd.*, 2009, **484**, p 196–202
18. F.F. Cardoso, A. Cremasco, R.J. Contieri, E.S.N. Lopes, C.R.M. Afonso, and R. Caram, Hexagonal Martensite Decomposition and Phase Precipitation in Ti–Cu Alloys, *Mater. Des.*, 2011, **32**, p 4608–4613
19. T. Luangvaranunt and P. Pripanapong, Pin-On-Disc Wear of Precipitation Hardened Titanium-Copper Alloys Fabricated by Powder Metallurgy, *Mater. Trans.*, 2012, **53**(3), p 518–523
20. T. Shirai, H. Tsuchiya, T. Shimizu, K. Ohtani, Y. Zen, and K. Tomita, Prevention of Pin Tract Infection with Titanium-Copper Alloys, *J. Biomed. Mater. Res. B*, 2009, **91**, p 373–380
21. I. Gurappa, Characterisation of Different Materials for Corrosion Resistance Under Simulated Body Fluid Conditions, *Mater. Charact.*, 2002, **49**, p 73–79
22. J. Liu, F. Li, C. Liu, H. Wang, B. Ren, K. Yang, and E. Zhang, Effect of Cu Content on the Antibacterial Activity of Titanium-Copper Sintered Alloys, *Mater. Sci. Eng. C*, 2014, **35**, p 392–400
23. T. Albrektsson and F. Isidor, Consensus Report of Session IV, *Proceedings of the First European Workshop on Periodontology*, N.P. Lang and T. Karring, Ed., Quintessence, London, 1994, p 365–369
24. T. Albrektsson and C. Johansson, Osteoinduction, Osteoconduction and Osseointegration, *Eur. Spine J.*, 2001, **10**, p 96–101
25. M. Yoshinari, Y. Oda, T. Kato, and K. Okuda, Influence of Surface Modifications to Titanium on Antibacterial Activity In Vitro, *Biomaterials*, 2001, **22**, p 2043–2048
26. D. Mareci, R. Chelariu, I. Dan, D.M. Gordin, and T. Gloriant, Corrosion Behaviour of Ti20Mo Alloy in Artificial Saliva, *J. Mater. Sci. Mater. Med.*, 2010, **21**, p 2907–2913
27. M. Sharma, A.V.R. Kumar, N. Singh, N. Adya, and B. Saluja, Electrochemical Corrosion Behavior of Dental/Implant Alloys in Artificial Saliva, *J. Mater. Eng. Perform.*, 2008, **17**, p 695–701
28. W.F. Ho, S.C. Wu, C.W. Lin, and S.K.H.C. Hsu, Electrochemical Behavior of Ti-20Cr-X Alloys in Artificial Saliva Containing Fluoride, *J. Appl. Electrochem.*, 2011, **41**, p 337–343
29. Y. Oshida, C.B. Sellers, K. Mirza, and F. Farzin-Nia, Corrosion of Dental Materials by Dental Treatment Agents, *Mater. Sci. Eng. C*, 2005, **25**, p 343–348
30. S. Kumar, T.S.N.S. Narayanan, and S.S. Kumar, Influence of Fluoride ion on the Electrochemical Behaviour of β -Ti Alloy for Dental Implant Application, *Corros. Sci.*, 2010, **52**, p 1721–1727
31. F. Xie, X. He, S. Cao, M. Mei, and X. Qu, Influence of Pore Characteristics on Microstructure, Mechanical Properties and Corrosion Resistance of Selective Laser Sintered Porous Ti–Mo Alloys for Biomedical Applications, *Electrochim. Acta*, 2013, **105**, p 121–129
32. W.R. Osorio, A. Cremasco, P.N. Andrade, A. Garcia, and R. Caram, Electrochemical Behavior of Centrifuged Cast and Heat Treated Ti–Cu Alloys for Medical Applications, *Electrochim. Acta*, 2010, **55**, p 759–770

33. A. Robin and J.P. Meirelis, Influence of Fluoride Concentration and pH on Corrosion Behavior of Titanium in Artificial Saliva, *J. Appl. Electrochem.*, 2007, **37**, p 511–517
34. J. Fojt, L. Joska, and J. Malek, Corrosion Behaviour of Porous Ti-39Nb Alloy for Biomedical Applications, *Corros. Sci.*, 2013, **71**, p 78–83
35. C. García, F. Martín, P. Tiedra, Y. Blanco, J.M.R. Roman, and M. Aparicio, Electrochemical Reactivation Methods Applied to PM Austenitic Stainless Steels Sintered in Nitrogen-Hydrogen Atmosphere, *Corros. Sci.*, 2008, **50**, p 687–697
36. I. Mutlu, Sinter-Coating Method for the Production of TiN-Coated Titanium Foam for Biomedical Implant Applications, *Surf. Coat. Technol.*, 2013, **232**, p 396–402
37. M. Nakagawa, S. Matsuya, and K. Udoh, Corrosion Behavior of Pure Titanium and Titanium Alloys in Fluoride-Containing Solutions, *Dent. Mater. J.*, 2001, **20**(4), p 305–314